Two-Phase Viscoelastic Jetting

Jiun-Der Yu[*]
Epson Research and Development, Inc.
3145 Porter Drive, Suite 104
Palo Alto, CA 94304

Shinri Sakai
Seiko Epson Corporation
Technology Platform Research Center
281 Fujimi, Fujimi-machi, Suwa-gun
Nagano-ken, 399-0293, Japan

J.A. Sethian[†]
Department of Mathematics
University of California, Berkeley
Berkeley, CA 94720

Abstract

A coupled finite difference algorithm on rectangular grids is developed for viscoelastic ink ejection simulations. The ink is modeled by the Oldroyd-B viscoelastic fluid model. The coupled algorithm seamlessly incorporates several things: (1) a coupled level set-projection method for incompressible immiscible two-phase fluid flows; (2) a higher-order Godunov type algorithm for the convection terms in the momentum and level set equations; (3) a simple first-order upwind algorithm for the convection term in the viscoelastic stress equations; (4) central difference approximations for viscosity, surface tension, and upper-convected derivative terms; and (5) an equivalent circuit model to calculate the inflow pressure (or flow rate) from dynamic voltage.

[*]The corresponding author.

[†]This author was supported in part by the Applied Mathematical Sciences subprogram of the Office of Energy Research, U.S. Department of Energy, under Contract Number DE-AC03-76SF00098, and the Division of Mathematical Sciences of the National Science Foundation.

1 Introduction

The goal of this work is to develop computational techniques which can be applied to two-phase viscoelastic flows in complex geometries. The fluid model considered in this work is the Oldroyd-B viscoelastic fluid model, in which both the dynamic viscosity and relaxation time are constant. Our purpose is to simulate two-phase immiscible incompressible flows in the presence of surface tension and density jump across the interface separating a viscoelastic fluid and from air, incorporated with a macroscopic slipping contact line model which describes the air-fluid-wall dynamics. The fluid interface between the air and the fluid is treated as an infinitely thin immiscible boundary, separating regions of different but constant densities and viscosities. The flow is axisymmetric, and for boundary conditions on solid walls we assume that both the normal and tangential component of the fluid velocity vanish; this is amended by the contact model at places where the interface meets walls. Here, we wish to be able to simulate air/wall/fluid interactions and such effects as interactions between geometry and viscoelastic forces. The computational model and algorithm are general enough to handle problems in which either of the two fluids is either viscoelastic or Newtonian.

Applications involving viscoelastic fluid jets are quite broad, and include such areas as microdispensing of bioactive fluids through high throughput injection devices, creation of cell attachment sites, scaffolds for tissue engineering, coatings and drug delivery systems for controlled drug release, and viscoelastic blood flow flow past valves.

We test and apply these algorithms in the context of ink jet plotters. Regular dye-based inks used in desktop printers are Newtonian, which means the relation between the stress tensor and the rate of deformation tensor at an instant is linear and not related to any other instant. The use of pigment-based inks at the end of the 1990's improved the color durability of a ink jet printout. Pigment-based inks and inks used in industrial printing applications are usually viscoelastic, i.e. the relation between the stress tensor and the rate of deformation tensor at an instant depends on the deformation history.

The typical structure of an ink jet nozzle is shown in Figure 1. The actual geometry is axisymmetric and is not drawn to scale. Ink is stored in a cartridge, and driven through the nozzle in response to a dynamic pressure at the lower boundary (nozzle inflow). The dynamics of incompressible viscoelastic fluid flow through the nozzle, coupled to surface tension effects along the ink-air interface and boundary conditions along the wall, act to determine the shape of the interface as it moves. A negative pressure at the nozzle inflow induces a backflow, which together with the capillary instability causes the bubble to pinch off. The bubble moves through the domain and usually separates into a major droplet and at least one small droplet (satellite).

1.1 Background

Several different numerical simulations of the Newtonian ink jet process have been performed in recent years, see, for example, Aleinov et al.[1], Sou et al.[22], and Yu et al.[28, 29]. Our methods make use of level set methods for tracking the fluid interface boundaries, coupled to projection methods to solving the associated fluid flows. A large number of background references for projection methods and level set methods are given in [28]; here we briefly mention the original paper on projection methods for incompressible flow by Chorin[8], second-order Godunov-type improvements by Bell, Colella, and Glaz[4], the finite-element approximate projection by Almgren et al.[2], and the extension of these techniques to quadrilateral grids (see, for example, Bell et al.[6]) and to moving quadrilateral grids (see Trebotich and Colella[26]). On the interface tracking side, level set methods, introduced in Osher and Sethian[15], rely in part on the theory of curve and surface evolution given in Sethian[18, 19] and on the link between front propagation and hyperbolic conservation laws discussed in Sethian[20]; these techniques recast interface motion as a time-dependent Eulerian initial value partial differential equation. For a general introduction and overview, see Sethian[21]. For details about projection methods and their coupling to level set methods, see Almgren et al.[2, 3], Bell et al.[4], Bell and Marcus[5], Chang et al.[7], Chorin[8], Puckett et al.[16], Sussman and Smereka[24], Sussman et al.[23, 25], and Zhu and Sethian[30]. On the viscoelastic side, in recent years there has been considerable interest in projection-type schemes for viscoelastic flow, see, for example, Trebotich et. al.[26]. A good overview of issues involved in simulating viscoelastic flows may be found in [11].

One of the most perplexing problems in viscoelastic flow is the limitations imposed on the Weissenberg number. Algorithms typically go unstable for a moderate range of Weissenberg numbers, and this has been the subject of considerable research: large stress levels, coupled to regimes of rapid changes are computationally difficult and cause many schemes, both finite difference and finite element, to go unstable. The problem is summarized in [14]: see [10] for a good review, as well as [26] and [13] for some recent work. An excellent introductory review of the mathematical and numerical issues may be found in [11].

1.2 Current Work

In previous work [28, 29], we have built numerical simulations of the ink jet process for Newtonian fluids using coupled level set and projection methods in both rectangular and arbitrary quadrilateral geometries. In this work, we extend these results to the viscoelastic regime. The coupled algorithm seamlessly incorporates several things: (1) a projection method to enforce the fluid incompressibility; (2) the level set methods to implicitly capture the moving interface; (3) a higher-order Godunov type algorithm for the convection terms in the momentum and level set equations; (4) a simple

first-order upwind algorithm for the convection term in the viscoelastic stress equations; (5) the central difference for viscosity, surface tension, and other upper-convected derivative terms; and (6) an equivalent circuit to calculate the inflow pressure (or flow rate) with given dynamic voltage.

We apply these techniques to perform a parameter study of the jetting ejection process under a range of viscoelastic relaxation parameters. Our results show the effect of viscoelastic parameters on the jetting process. In particular, they demonstrate that the ink elasticity has a dramatic effect on droplet ejection and formation. For Newtonian fluids under reasonable configurations and parameters, pressure bursts in the ink chamber expel ink through the nozzle which then pinches off and breaks into droplets. As the ink characteristics become more viscoelastic, droplets become longer in shape, smaller in volume, and pinch off later. In the case of larger viscoelastic relaxation times, droplets are pulled back by the combination of elastic effects and surface tension and cannot be ejected.

In addition, we analyze the effectiveness of our approach under increasing Weissenberg number, and try to lay out the regimes in which it is effective.

2 Level Set Formulation

2.1 Equations of Motion

Fluid #1 (ink) is a viscoelastic fluid. We use the Oldroyd-B viscoelastic fluid model to present our algorithm. Hence fluid #1 is governed by

$$\begin{aligned} \rho_1 \frac{D\boldsymbol{u}_1}{Dt} &= -\nabla p_1 + \nabla \cdot (2\mu_1 \mathcal{D}_1) + \nabla \cdot \boldsymbol{\tau}_1 \ , \qquad \nabla \cdot \boldsymbol{u}_1 = 0 \ , \\ \frac{D\boldsymbol{\tau}_1}{Dt} &= \boldsymbol{\tau}_1 \cdot (\nabla \boldsymbol{u}_1) + (\nabla \boldsymbol{u}_1)^T \cdot \boldsymbol{\tau}_1 - \frac{1}{\lambda_1} (\boldsymbol{\tau}_1 - 2\mu_{p1} \mathcal{D}_1) \ . \end{aligned} \tag{1}$$

Fluid #2 (air) is governed by the incompressible Navier-Stokes equations, i.e.

$$\rho_2 \frac{D\boldsymbol{u}_2}{Dt} = -\nabla p_2 + \nabla \cdot (2\mu_2 \mathcal{D}_2) \ , \qquad \nabla \cdot \boldsymbol{u}_2 = 0 \ . \tag{2}$$

In the above equations,

$$\begin{aligned} \mathcal{D}_i = \frac{1}{2} \left[\nabla \boldsymbol{u}_i + (\nabla \boldsymbol{u}_i)^T \right] \ , \qquad i = 1, 2 \ , \\ \boldsymbol{u}_i = u_i \boldsymbol{e}_r + v_i \boldsymbol{e}_z \ , \qquad i = 1, 2 \end{aligned} \tag{3}$$

are the rate of deformation tensor and the fluid velocity, respectively, $\frac{D\boldsymbol{u}_i}{Dt} = [\frac{\partial}{\partial t} + (\boldsymbol{u}_i \cdot \nabla)]\boldsymbol{u}_i$ is the Lagrangian time derivative, p_i the pressure, $\boldsymbol{\tau}_1$ the viscoelastic stress tensor of fluid #1, ρ_i the density, μ_i the dynamic viscosity, λ_1 the viscoelastic relaxation time of fluid #1, μ_{p1} the solute dynamic viscosity of fluid #1. The subscript $i = 1, 2$ is used to denote the variable or constant in fluid #1 (ink) or fluid #2 (air).

We would like to make several comments here. First, since the second fluid is assumed to be the air, which is Newtonian, the viscoelastic stress tensor $\boldsymbol{\tau}_2$ vanishes in fluid #2. The dynamic viscosity μ_1 is actually the dynamic viscosity of the ink solvent, which is usually water. Second, the first three terms together in (1) $\frac{D\boldsymbol{\tau}_1}{Dt} - \boldsymbol{\tau}_1 \cdot (\nabla \boldsymbol{u}_1) - (\nabla \boldsymbol{u}_1)^T \cdot \boldsymbol{\tau}_1$ constitute the upper-convected time derivative of the viscoelastic stress tensor. It is used in the Oldroyd-B model to guarantee the material frame indifference. It can be also deemed as the Lagrangian time derivative of the Kirchoff-Piola stress tensor of the second kind. Third, because the size of typical ink jet print heads is small, the gravity term is not important and is omitted. The inclusion of a gravity term does not change any part of the numerical schemes described in the next sections. Finally, the numerical schemes work equally well for cases in which both fluids are viscoelastic.

The boundary conditions at the interface of the two phases are the continuity of the velocity and the jump condition

$$(2\mu_1 \mathcal{D} - 2\mu_2 \mathcal{D}) \cdot \boldsymbol{n} = (p_1 - p_2 + \sigma\kappa)\boldsymbol{n} \ , \tag{4}$$

where $\boldsymbol{n}$ is the unit normal to the interface drawn from fluid #2 to fluid #1 and κ is the curvature of the interface.

We use the level set method to trace the interface (see Osher and Sethian[15]). The interface is the zero level of the level set function ϕ, chosen so that $\phi(x, y)$ is less than (greater than) 0 if (x, y) is in fluid 2 (fluid 1), vanishes on the interface, and is initialized as the signed distance to the interface. The unit normal on the interface can be expressed in terms of ϕ by $\boldsymbol{n} = \left.\frac{\nabla\phi}{|\nabla\phi|}\right|_{\phi=0}$ and $\kappa = \nabla \cdot \left.\left(\frac{\nabla\phi}{|\nabla\phi|}\right)\right|_{\phi=0}$. Finally, let $\boldsymbol{u} = \boldsymbol{u}_1$, $\boldsymbol{\tau} = \boldsymbol{\tau}_1$, $p = p_1$, and $\mathcal{D} = \mathcal{D}_1$ for $\phi > 0$, and $\boldsymbol{u} = \boldsymbol{u}_2$, $\boldsymbol{\tau} = \boldsymbol{\tau}_2$, $p = p_2$, and $\mathcal{D} = \mathcal{D}_2$ for $\phi < 0$. The governing equations for the two-phase flow and the boundary condition at the interface can then be re-written as

$$\nabla \cdot \boldsymbol{u} = 0 \ , \tag{5}$$

$$\rho(\phi)\frac{D\boldsymbol{u}}{Dt} = -\nabla p + \nabla \cdot (2\mu(\phi)\mathcal{D}) + \nabla \cdot \boldsymbol{\tau} - \sigma\kappa(\phi)\delta(\phi)\nabla\phi \ , \tag{6}$$

$$\frac{D\boldsymbol{\tau}}{Dt} = \boldsymbol{\tau} \cdot (\nabla \boldsymbol{u}) + (\nabla \boldsymbol{u})^T \cdot \boldsymbol{\tau} - \frac{1}{\lambda(\phi)}(\boldsymbol{\tau} - 2\mu_p(\phi)\mathcal{D}) \tag{7}$$

where δ is the Dirac delta function and ρ, μ, λ, and μ_p are taken as $\rho_1(\rho_2)$, $\mu_1(\mu_2)$, $\lambda_1(0)$, and $\mu_{p1}(0)$ for $\phi \geq 0 (\phi < 0)$. The fact that the surface tension can be written as a body force concentrated at the interface greatly reduces the difficulty involved in solving two-phase fluid flows.

To make the governing equations dimensionless, we choose the following definitions

$$\begin{aligned} &x = Lx', \qquad y = Ly', \qquad t = \frac{L}{U}t', \\ &p = \rho_1 U^2 p', \qquad \boldsymbol{u} = U\boldsymbol{u}', \qquad \boldsymbol{\tau} = \rho_1 U^2 \boldsymbol{\tau}' \ , \\ &\rho = \rho_1 \rho', \qquad \mu = \mu_1 \mu', \qquad \lambda = \frac{L}{U}\lambda', \qquad \mu_p = \mu_1 \mu_p' \ , \end{aligned} \tag{8}$$

where the primed quantities are dimensionless and L, U, ρ_1, μ_1 are respectively the characteristic length, characteristic velocity, density of fluid #1, and solvent dynamic viscosity of fluid #1.

Substituting the above into equations (5) and (6), and dropping the primes, we have

$$\nabla \cdot \boldsymbol{u} = 0 \ , \tag{9}$$

$$\frac{D\boldsymbol{u}}{Dt} = -\frac{1}{\rho(\phi)}\nabla p + \frac{1}{\rho(\phi)Re}\nabla \cdot (2\mu(\phi)\mathcal{D}) - \frac{1}{\rho(\phi)We}\kappa(\phi)\delta(\phi)\nabla\phi + \nabla \cdot \boldsymbol{\tau} \ , \tag{10}$$

$$\frac{D\boldsymbol{\tau}}{Dt} = \boldsymbol{\tau} \cdot (\nabla \boldsymbol{u}) + (\nabla \boldsymbol{u})^T \cdot \boldsymbol{\tau} - \frac{1}{\lambda(\phi)}\left(\boldsymbol{\tau} - 2\frac{\mu_p(\phi)}{Re_p}\mathcal{D}\right) \tag{11}$$

where the density ratio, viscosity ratio, normalized relaxation time, Reynolds number of the solvent, Weber number, and Reynolds number of the solute are defined by

$$\rho(\phi) = \begin{bmatrix} 1 & \text{if } \phi \geq 0 \\ \rho_2/\rho_1 & \text{if } \phi < 0 \end{bmatrix} \quad \mu(\phi) = \begin{bmatrix} 1 & \text{if } \phi \geq 0 \\ \mu_2/\mu_1 & \text{if } \phi < 0 \end{bmatrix} \quad \lambda(\phi) = \begin{bmatrix} 1 & \text{if } \phi \geq 0 \\ 0 & \text{if } \phi < 0 \end{bmatrix}$$

and

$$Re = \frac{\rho_1 UL}{\mu_1} \ , We = \frac{\rho_1 U^2 L}{\sigma} \ , Re_p = \frac{\rho_1 UL}{\mu_{p1}} \ .$$

Since the interface moves with the fluid, the evolution of the level set is governed by

$$\frac{\partial \phi}{\partial t} + \boldsymbol{u} \cdot \nabla \phi = 0 \ . \tag{12}$$

We choose this form because the interface is advected with the flow.

Since equations (2.1), (9), and (10) are expressed in terms of the vector notation, they assume the same form in Cartesian coordinates and axisymmetric coordinates.

2.2 Boundary Conditions and Contact Models

On solid walls, we assume that both the normal and tangential components of the velocity vanish (this must be amended at the triple point). At both inflow and outflow, our formulation allows us to prescribe either the velocity

$$\boldsymbol{u} = \boldsymbol{u}^{BC} \tag{13}$$

or the pressure boundary condition

$$p = p^{BC} \ , \quad \frac{\partial \boldsymbol{u}}{\partial \boldsymbol{n}} = 0 \ , \tag{14}$$

where $\boldsymbol{n}$ denotes the unit normal to the inflow or outflow boundary. Boundary conditions for the viscoelastic stresses, when needed, are implemented using the zeroth-order extrapolation suggested by Trebotich et al.[26].

To numerically simulate the ejection of ink droplets, one needs to prescribe a velocity or pressure at the inflow to the nozzle. However, only the input voltage to the piezoelectric actuator is known. The equivalent circuit model by Sakai[17, 27] is employed to handle the problem. The equivalent circuit, which includes the effect of ink cartridge, supply channel, vibration plate, and piezoelectric actuator, simulates the ink velocity and pressure at nozzle inflow with a given dynamic voltage. The equivalent circuit receives as an input the dynamic voltage to be applied to the piezoelectric PZT actuator and simulates the ink behavior under the influence of ink cartridge, supply channel, vibration plate, and PZT actuator. The circuit calculates an inflow pressure that drives the CFD code. The CFD code then solves the governing partial differential equations for the fluid velocity, pressure, interface position, and viscoelastic stresses, and feeds back the ink flow rate to the equivalent circuit. The sequence is repeated as long as needed. A typical driving voltage pattern is as shown in Figures 3. The driving voltage is such that the ink is first pulled back, pushed and fired, and then pulled back to get ready for the next ejection.

At the triple point, where air and ink meet at the solid wall, we adopt the slipping contact line model discussed in detail in [28]. The contact angle θ is the angle made by the air-liquid interface and the solid, measured from the side of the liquid by approaching the contact line (i.e. the triple point) as closely as possible. The advancing critical contact angle θ_a and receding critical contact angle θ_r are the maximum and minimum contact angles which allow the triple point to stay. The velocity v_B is the tangential velocity of the point on the interface at $0.5\mu m$ from the triple point. The triple point is allowed to move toward the air side if $\theta \geq \theta_a$ and $v_B > 0$. The triple point is allowed to move toward the liquid side if $\theta \leq \theta_r$ and $v_B < 0$. If the triple point is not allowed to move, the boundary condition at the solid wall is the no-slip condition. If the triple point is allowed to move, the no-slip condition in a close vicinity of the triple point is switched to the free slip condition and an extra surface tension force is added to accelerate the triple point. For Epson's dye-based ink and print head nozzle wall, θ_a and θ_r are about 80° and 20°.

3 Numerical Algorithms on Rectangular Grids

In the paper, the superscript n (or $n+1$) denotes the time step, i.e.

$$\boldsymbol{u}^n = \boldsymbol{u}(t = n\Delta t) \tag{15}$$

and so on. Given quantities $\boldsymbol{u}^n, p^n, \phi^n, \boldsymbol{\tau}^n$, the purpose is to obtain $\boldsymbol{u}^{n+1}, p^{n+1}, \phi^{n+1}, \tau^{n+1}$ which satisfy the condition of incompressibility (9). The explicit algorithm we describe will be first-order accurate in time and second-order accurate in space.

3.1 Temporal Discretization

The boundary condition on the nozzle wall stems from the proposed contact model. The inflow pressure at t^{n+1} is given by the equivalent circuit.

3.1.1 Level set update

The level set is updated by

$$\phi^{n+1} = \phi^n - \Delta t \left[\boldsymbol{u} \cdot \nabla \phi\right]^{n+1/2} \ . \tag{16}$$

The time-centered advection term $\left[\boldsymbol{u} \cdot \nabla \phi\right]^{n+1/2}$ is evaluated using an explicit predictor-corrector scheme that requires only the available data at t^n; more detail is given in section 3.2. That is, once ϕ^{n+1} is obtained, we compute $\phi^{n+1/2}$ by using the update rule

$$\phi^{n+1/2} = \frac{1}{2}\left(\phi^n + \phi^{n+1}\right) \ . \tag{17}$$

3.1.2 Explicit time integration for momentum equations

An explicit discretization in time is employed to integrate the momentum equations:

$$\begin{aligned} &\frac{\boldsymbol{u}^{n+1} - \boldsymbol{u}^n}{\Delta t} + \left[\left(\boldsymbol{u} \cdot \nabla\right)\boldsymbol{u}\right]^{n+1/2} \\ &= -\frac{1}{\rho(\phi^{n+1/2})}\nabla p^{n+1} + \frac{1}{\rho(\phi^{n+1/2})Re}\nabla \cdot \left[2\mu(\phi^{n+1/2})\mathcal{D}^n\right] \\ &\quad + \nabla \cdot \boldsymbol{\tau}^n - \frac{1}{\rho(\phi^{n+1/2})We}\left[\kappa(\phi)\delta(\phi)\nabla\phi\right]^{n+1/2} \ . \end{aligned} \tag{18}$$

If we define

$$\begin{aligned} \boldsymbol{u}^* = \boldsymbol{u}^n + \Delta t \Big\{ &- \left[\left(\boldsymbol{u} \cdot \nabla\right)\boldsymbol{u}\right]^{n+1/2} + \frac{1}{\rho(\phi^{n+1/2})Re}\nabla \cdot \left[2\mu(\phi^{n+1/2})\mathcal{D}^n\right] \\ &\nabla \cdot \boldsymbol{\tau}^n - \frac{1}{\rho(\phi^{n+1/2})We}\left[\kappa(\phi)\delta(\phi)\nabla\phi\right]^{n+1/2}\Big\} \ , \end{aligned} \tag{19}$$

the time-discretized momentum equations can be written as

$$\boldsymbol{u}^{n+1} = \boldsymbol{u}^* - \frac{\Delta t}{\rho(\phi^{n+1/2})}\nabla p^{n+1} \ . \tag{20}$$

We apply a second-order explicit Godunov scheme for the advection term and the central difference for the viscosity term in (19). They will be explained later. It is clear that the determination of $\boldsymbol{u}^*$ needs only values at time step n.

3.1.3 Projection for $\boldsymbol{u}^{n+1}$

To satisfy the incompressibility condition for time step $n+1$, we apply the divergence operator on both sides of (20). Since $\nabla \cdot \boldsymbol{u}^{n+1} = 0$, we have

$$\nabla \cdot \boldsymbol{u}^* = \nabla \cdot \left(\frac{\Delta t}{\rho(\phi^{n+1/2})}\nabla p^{n+1}\right) \ . \tag{21}$$

The projection equation (21) is elliptic. It reduces to a Poisson equation if the density ratio $\rho(\phi^{n+1/2})$ is a constant. After the pressure p^{n+1} is solved from equation (21), the velocity field $\boldsymbol{u}^{n+1}$ can be obtained by (20).

To simplify the implementation for arbitrary geometries, we use a finite element projection of the form

$$\int_\Omega \boldsymbol{u}^* \cdot \nabla\psi d\boldsymbol{x} = \int_\Omega \frac{\Delta t}{\rho(\phi^{n+1/2})} \nabla p^{n+1} \cdot \nabla\psi d\boldsymbol{x} + \int_{\Gamma_1} \psi \boldsymbol{u}^{BC} \cdot \boldsymbol{n} dS \ , \tag{22}$$

where ψ is the finite element weighting function, Γ_1 denotes all the boundary with inflow or outflow, and $\boldsymbol{u}^{BC}$ is the given boundary velocity. It is easy to see by the divergence theorem that the implied boundary condition at Γ_1 is

$$\frac{\Delta t}{\rho(\phi^{n+1/2})} \frac{\partial p^{n+1}}{\partial n} = \left(\boldsymbol{u}^* - \boldsymbol{u}^{BC}\right) \cdot \boldsymbol{n} \ . \tag{23}$$

The choice of the weighting function, as well as the approximation for the pressure and velocity, is flexible. In our implementation, the weighting function and the pressure are chosen to be piecewise bilinear, and the velocity to be piecewise constant.

3.1.4 Mixed algorithm for the viscoelastic stress equations

In the projection step, we obtain both the new pressure and velocity. The time-centered velocity at cell centers can be calculated by

$$\boldsymbol{u}^{n+1/2} = (\boldsymbol{u}^n + \boldsymbol{u}^{n+1})/2 \ . \tag{24}$$

We use a mixed algorithm to integrate the viscoelastic stress equations in time:

$$\begin{aligned} \frac{\boldsymbol{\tau}^{n+1} - \boldsymbol{\tau}^n}{\Delta t} = \ & -(\boldsymbol{u}^{n+1/2} \cdot \nabla)\boldsymbol{\tau}^n + \boldsymbol{\tau}^n \cdot (\nabla \boldsymbol{u}^{n+1/2}) + (\nabla \boldsymbol{u}^{n+1/2})^T \cdot \boldsymbol{\tau}^n \\ & - \frac{1}{\lambda(\phi^{n+1/2})} \left(\boldsymbol{\tau}^{n+1} - 2\frac{\mu_p(\phi^{n+1/2})}{Re_p} \mathcal{D}^{n+1/2} \right) \ , \end{aligned} \tag{25}$$

where $\boldsymbol{u}^{n+1/2}$ is the time-centered velocity field at cell centers as obtained in (24). It is noted that the mixed algorithm is explicit on the upper-convected derivative terms and the solute viscosity term, but is implicit on the relaxation term. After arrangement, we have

$$\begin{aligned} & \left(1 + \frac{\Delta t}{\lambda_p(\phi^{n+1/2})}\right) \boldsymbol{\tau}^{n+1} \\ & = \boldsymbol{\tau}^n + \Delta t \left[-(\boldsymbol{u}^{n+1/2} \cdot \nabla)\boldsymbol{\tau}^n + \boldsymbol{\tau}^n \cdot (\nabla \boldsymbol{u}^{n+1/2}) + (\nabla \boldsymbol{u}^{n+1/2})^T \cdot \boldsymbol{\tau}^n \right] + \frac{2\Delta t \mu_p(\phi^{n+1/2})}{\lambda(\phi^{n+1/2}) Re_p} \mathcal{D}^{n+1/2} \ . \end{aligned} \tag{26}$$

3.1.5 Re-initialization of the level set

To correctly capture the interface and accurately calculate the surface tension, the level set function should remain a signed distance function to the interface as the calculation unfolds. However, if we update the level set by (9), it will not remain as such. Instead, we periodically stop the simulation and recreate a new level set function ϕ which is the signed distance function, i.e. $|\nabla\phi| = 1$, without changing the zero level set of the original level set function. In this work, we use a two-dimensional contour plotting algorithm to locate the zero level set and then calculate the exact distances from the zero level set to cell centers.

3.2 Advection Terms in Navier-Stokes and Level Set Equations

Referring to Figures 2a and 2b, the velocity components $\boldsymbol{u}^n_{i,j}$ and the level set function values $\phi^n_{i,j}$ are located at cell centers, and the pressure $p^n_{i,j}$ is located at grid points. The time-centered edge velocities and level set function values (also called the "predictors"), such as $\boldsymbol{u}^{n+1/2}_{i+1/2,j}$, $\phi^{n+1/2}_{i+1/2,j}$, and so on, are located at the middle point of each edge. The algorithm for the advection terms is based on the unsplit, second-order Godunov type upwind method introduced by Colella [9]. It is a cell-centered predictor-corrector scheme.

In the predictor step, we use Taylor's series to extrapolate the velocity and level set at t^n to obtain their cell edge values at $t^{n+1/2}$. The partial derivative with respect to time in the extrapolation is substituted by the Navier-Stokes equations or by the level set convection equation. There are two extrapolated velocities and level sets for each cell edge. For example, for the cell edge between cells i, j and $i+1, j$, one can extrapolate from the left and have

$$\begin{aligned} \boldsymbol{u}^{n+1/2,L}_{i+1/2,j} &= \boldsymbol{u}^n_{i,j} + \frac{\Delta r}{2}\boldsymbol{u}^n_{r,i,j} + \frac{\Delta t}{2}\boldsymbol{u}^n_{t,i,j} \\ &= \boldsymbol{u}^n_{i,j} + \frac{1}{2}\left(\Delta r - \Delta t u^n_{i,j}\right)\boldsymbol{u}^n_{r,i,j} - \frac{\Delta t}{2}\left(\widehat{v\boldsymbol{u}}_z\right)_{i,j} + \frac{\Delta t}{2}\boldsymbol{F}^n_{i,j} \ , \end{aligned} \tag{27}$$

where

$$\boldsymbol{F}^n_{i,j} = \left\{ -\frac{1}{\rho(\phi)}\nabla p + \frac{1}{\rho(\phi)Re}\nabla\cdot(2\mu(\phi)\mathcal{D}) + \nabla\cdot\boldsymbol{\tau} - \frac{1}{\rho(\phi)We}\kappa(\phi)\delta(\phi)\nabla\phi \right\}^n_{i,j} \tag{28}$$

and extrapolate from the right to produce

$$\begin{aligned} \boldsymbol{u}^{n+1/2,R}_{i+1/2,j} &= \boldsymbol{u}^n_{i+1,j} - \frac{1}{2}\boldsymbol{u}^n_{\xi,i+1,j} + \frac{\Delta t}{2}\boldsymbol{u}^n_{t,i+1,j} \\ &= \boldsymbol{u}^n_{i+1,j} - \left(\frac{1}{2} + \frac{\Delta t}{2J_{i+1,j}}\bar{u}^n_{i+1,j}\right)\boldsymbol{u}^n_{\xi,i+1,j} - \frac{\Delta t}{2J_{i+1,j}}\left(\bar{v}\boldsymbol{u}_\eta\right)^n_{i+1,j} + \frac{\Delta t}{2}\boldsymbol{F}^n_{i+1,j} \ . \end{aligned} \tag{29}$$

We use the monotonicity-limited 4th-order central difference for the evaluation of the normal slopes, which is $\boldsymbol{u}^n_{r,i,j}$ in this case. The limiting is done on each component of the velocity at t^n separately. The transverse derivative term $(\widehat{v\boldsymbol{u}}_z)_{i,j}$ is evaluated by first extrapolating $\boldsymbol{u}$ to the

transverse faces from the cell center, using normal derivatives only, and then applying the Godunov type upwinding.

In the corrector step, we compute the Godunov upwind velocities which are then differenced to approximate the advection terms. The detail can be found in Yu et al.[28].

The obtained edge velocities are, in general, not divergence-free. An intermediate marker-and-cell (MAC) projection may be applied to make all the normal edge velocities divergence-free. Suppose q is a function which is smooth enough and $\boldsymbol{u}^e$ the edge velocities obtained after applying the Godunov procedure. We want

$$\boldsymbol{u}^e - \frac{1}{\rho(\phi^n)}\nabla q \tag{30}$$

to be divergence-free. By taking the divergence of (30), we have

$$\nabla \cdot \left(\frac{1}{\rho(\phi^n)}\nabla q\right) = \nabla \cdot \boldsymbol{u}^e \ . \tag{31}$$

The boundary condition for the intermediate projection should be compatible with the physical boundary conditions. On solid walls, $\boldsymbol{u} \cdot \boldsymbol{n} = 0$, which is already used in the construction of the edge velocity $\boldsymbol{u}^e$; thus, we have a homogeneous Neumann boundary condition on q, namely $\frac{\partial q}{\partial n} = 0$. At the inflow or outflow, if a velocity is prescribed, it is again a homogeneous Neumann boundary condition on q, since the given velocity at $t^{n+1/2}$ has been included in obtaining $\boldsymbol{u}^e$. If a pressure is given, the corresponding condition on q is

$$q = \frac{\Delta t}{2}\Delta p^{boundary} \ , \tag{32}$$

where the factor 2 in the denominator appears because the edge velocity is time-centered.

After $q_{i,j}$ is solved, we replace all the normal edge velocities by

$$\begin{aligned} u^{n+1/2}_{i+1/2,j} &\leftarrow u^{n+1/2}_{i+1/2,j} - \frac{1}{(\rho(\phi))_{i+1/2,j}}\frac{q_{i+1,j} - q_{i,j}}{\Delta r} \ , \\ v^{n+1/2}_{i,j+1/2} &\leftarrow v^{n+1/2}_{i,j+1/2} - \frac{1}{(\rho(\phi))_{i,j+1/2}}\frac{q_{i,j+1} - q_{i,j}}{\Delta z} \ . \end{aligned} \tag{33}$$

3.3 Spacial Discretization of the Viscoelastic Stress Terms

3.3.1 Evaluation of the advection term

Terms in the time-discretized equation (26) need to be discretized differently in space. The first term in the square bracket is a convection term. The following simple first-order upwind algorithm is used to evaluate the term on uniform rectangular grids:

$$\begin{aligned} (\boldsymbol{u}^{n+1/2} \cdot \nabla)\boldsymbol{\tau}^n = {} & \max(u^{n+1/2}_{i,j}, 0)\frac{\boldsymbol{\tau}^n_{i,j} - \boldsymbol{\tau}^n_{i-1,j}}{\Delta r} + \min(u^{n+1/2}_{i,j}, 0)\frac{\boldsymbol{\tau}^n_{i+1,j} - \boldsymbol{\tau}^n_{i,j}}{\Delta r} \\ & + \max(v^{n+1/2}_{i,j}, 0)\frac{\boldsymbol{\tau}^n_{i,j} - \boldsymbol{\tau}^n_{i,j-1}}{\Delta z} + \min(v^{n+1/2}_{i,j}, 0)\frac{\boldsymbol{\tau}^n_{i,j+1} - \boldsymbol{\tau}^n_{i,j}}{\Delta z} \ . \end{aligned} \tag{34}$$

3.3.2 Evaluation of the upper-convected derivative term

The second and third terms in the upper-convected derivative of equation (26), as well as the viscosity term, are discretized using a central difference approximation. To illustrate how we evaluate the two upper-convected derivative terms, we expand these derivatives. Since these two terms are similar, only one term will be shown here. In axi-symmetric coordinate systems, the second term of the upper-convected derivative can be expanded and expressed in the diadic form

$$\begin{aligned}[\boldsymbol{\tau}^n \cdot (\nabla \boldsymbol{u}^{n+1/2})] = (u_{,r}^{n+1/2}\tau_{rr}^n + u_{,z}^{n+1/2}\tau_{rz}^n)\boldsymbol{e}_r\boldsymbol{e}_r + (v_{,r}^{n+1/2}\tau_{rr}^n + v_{,z}^{n+1/2}\tau_{rz}^n)\boldsymbol{e}_r\boldsymbol{e}_z \\ +(u_{,r}^{n+1/2}\tau_{rz}^n + u_{,z}^{n+1/2}\tau_{zz}^n)\boldsymbol{e}_z\boldsymbol{e}_r + (v_{,r}^{n+1/2}\tau_{rz}^n + v_{,z}^{n+1/2}\tau_{zz}^n)\boldsymbol{e}_z\boldsymbol{e}_z + \frac{u^{n+1/2}}{r}\tau_{\theta\theta}^n\boldsymbol{e}_\theta\boldsymbol{e}_\theta \ .\end{aligned} \tag{35}$$

The value of the upper-convected terms is evaluated at cell centers by the use of central differences. For example, omitting the superscripts $^{n+1/2}$ and ^{n} for simplicity, we have

$$(u_{,r}\tau_{rr} + u_{,z}\tau_{rz})_{i,j} = \frac{u_{i+1,j} - u_{i-1,j}}{2\Delta r}\tau_{rr,i,j} + \frac{u_{i,j+1} - u_{i,j-1}}{2\Delta z}\tau_{rz,i,j} \ . \tag{36}$$

3.4 Interface Thickness and Time Step

Because of the numerical difficulty caused by the Dirac delta function and by the sharp change of ρ and ν across the free surface, the Heaviside and Dirac delta functions are replaced by smoothed functions (see Sussman et al.[23] and Yu et al.[28]). The interface thickness is 2ϵ, where the parameter ϵ is related to the mesh size by $\epsilon = \frac{\alpha}{2}(\Delta r + \Delta z)$. The thickness of the interface reduces as we refine the mesh. In this work, α is set to be 1.5.

Since the temporal discretization is explicit, the time step Δt is constrained by the CFL condition, surface tension, viscosity, and total acceleration

$$\begin{aligned}\Delta t < \min_{i,j}\Bigg[&\frac{\Delta r}{|u| + [2(\tau_{rr} + 1/\lambda Re)]^{1/2}} \ , \frac{\Delta z}{|v| + [2(\tau_{zz} + 1/\lambda Re)]^{1/2}} \ , \\ &\sqrt{We\frac{\rho_1 + \rho_2}{8\pi}}h^{3/2} \ , \frac{Re}{2}\frac{\rho^n}{\mu^n}\left(\frac{1}{\Delta r^2} + \frac{1}{\Delta z^2}\right)^{-1} \ , \sqrt{\frac{2h}{|\boldsymbol{F}|}}\Bigg] \ ,\end{aligned} \tag{37}$$

where $h = \min(\Delta r, \Delta z)$ and $\boldsymbol{F}$ is defined in (28).

4 Numerical Results

4.1 Convergence study

For a numerical example of the viscoelastic ink jet simulation and convergence study, we consider a typical nozzle as in Figure 1. The diameter is 25 microns at the opening and 49.5 microns at the bottom. The length of the nozzle opening part, where the diameter is 25 microns, is 26 microns. The slant part is 55 microns and the bottom part is 7.5 microns.

The inflow pressure is given by an equivalent circuit which simulates the effect of the ink cartridge, supply channel, vibration plate, PZT actuator, applied voltage, and the ink inside the channel and cartridge. We assumed that the input dynamic voltage is given by Figure 3 with the peak voltage at ± 11.15 volts. The corresponding inflow pressure for each simulated cases will be shown together with the droplet shapes in the next subsection. The outflow pressure at the top of the solution domain is set to zero.

The solution domain was chosen to be $\{(r,z)|0 \le r \le 27.3\mu m\ , 0 \le z \le 379.7\mu m\}$. Since the slant part of the nozzle wall is not parallel to the coordinate axes, we applied the "method of obstacle cells" (see Griebel et al.[12]) in discretizing the nozzle geometry using homogeneous rectangular cells. As a result, the nozzle wall has a staircase pattern (see Fig. 4). A better approximation would result from using a body-fitted quadrilateral mesh. However, it is demonstrated in [29] that the difference between using a staircase representation vs. a body-fitted mesh, while important for small-scale boundary effects, is not significant in terms of computing the pinch-off time, bubble velocity, and satellite formation. We shall extend our methodology to general quadrilateral grids elsewhere.

The advancing and receeding contact angles are taken to be 80° and 20°, respectively. The initial meniscus is assumed to be flat and 3.5 microns lower than the nozzle opening.

For the purpose of normalization, we chose the nozzle opening diameter (25 microns) to be the length scale and 6 m/sec to be the velocity scale. The normalized solution domain is hence $\{(r,z)|0 \le r \le 1.09\ , 0 \le z \le 15.19\}$. The density, solvent viscosity, solute viscosity, and surface tension of the ink we consider are approximately

$$\begin{aligned} &\rho_1 = 1070\ Kg/m^3\ , \qquad \mu_1 = 1.783 \times 10^{-3}\ Kg/m \cdot sec\ , \\ &\mu_p = 1.783 \times 10^{-3}\ Kg/m \cdot sec\ , \qquad \sigma = 0.0396\ Kg/sec^2\ . \end{aligned} \tag{38}$$

We hence have the following non-dimensional parameters

$$Re = 90.\ , \qquad We = 24.3\ , \qquad Re_p = 90\ . \tag{39}$$

The density and viscosity of air are

$$\rho_2 = 1.225\ Kg/m^3\ , \qquad \mu_2 = 1.77625 \times 10^{-3}\ Kg/m \cdot sec\ . \tag{40}$$

To check the convergence of our code for the case of $\lambda = 0.4$, we list in Tables 1, 2, and 3 the time of droplet pinch off, droplet head velocity, and droplet volume obtained from our code using various meshes.

It is seen that the 25×350 mesh does not conserve mass well. This is because the widest part of the ink droplet is only 7 to 8 cells wide. On such coarse meshes, level set methods incur substantial mass loss. While remedies have been proposed, they typically maintain global mass conservation

but suffer from local mass loss. The most effective remedy is a careful attention to re-initialization issues, higher order schemes, and sufficient grid resolutions, see Sethian [21].

4.2 Visco-elastistic Ink Jet

Simulation results (droplet shapes and inflow pressures) for various normalized relaxation times $\lambda = 0, 0.4, 1.0, 3.0$ are plotted in Fig. 5 to Fig. 10. The case with $\lambda = 0$ is just the case of Newtonian ink with a dynamic viscosity $3.566 \times 10^{-3}\ Kg/m \cdot sec.$ It is noted that the major droplet in the last graph of Fig. 5 has already passed the end of the solution domain and hence can not be seen.

The inflow pressures shown in Fig. 6 and 10 reflect the reaction of a typical nozzle-ink channel-actuator-cartridge system to the applied voltage and are also related to fluid properties. The inflow pressures contain a higher frequency signal. It is the fundamental natural frequency of the system, which is five to six times higher than the driving voltage frequency in this case.

Comparing results in Fig. 5 to 10, we see that, although the ink elasticity does not change the inflow pressure by much, it dramatically influences the droplet jettability, pinch off, shape, speed, and size. It is obvious from the droplet shape figures that the droplet pinches off later, becomes longer in shape and smaller in volume, and slows down when the ink elasticity becomes stronger. Since a long droplet usually separates into a major droplet and one or more satellites due to the capillary instability, a longer and slender shape at pinch off tends to result in a smaller major droplet and more satellites, which is unfavorable in ink jet applications. The droplet sizes for the Newtonian case, $\lambda = 0.4$, and $\lambda = 1.0$ are respectively 11.89, 10.98, and 7.66 pico liters. The results in Fig. 8 and Fig. 9 show that, at the given peak voltage ($\pm 11.15 volts$) and dynamic pattern, the ink droplet can not be ejected when $\lambda > 1$. In the $\lambda = 3.0$ case, the droplet is at first formed and pushed out, but does not get enough momentum to pinch off. It is finally pulled back by the elastic effect and surface tension. To eject highly viscoelastic ink, one has to either apply higher peak voltage or invent a new dynamic voltage pattern.

The simulated relation between the droplet volume and the peak voltage of the driving signal is plotted in Fig. 11, where the dash line is for Newtonian ink and the solid line for viscoelastic ink ($\lambda = 0.4$). The linear volume-peak voltage relation for Newtonian ink was first reported by Yu et. al.[28]. The linearity facilitates the control of drop-on-demand ink jet devices. It is interesting to see that the linear relation between the peak voltage and droplet volume remains similar for viscoelastic ink based on the Oldroyd-B model. We suspect a nonlinear viscoelastic model may destroy the linearity; however, this relationship will be pursued elsewhere.

In order to understand the range of Weissenberg numbers in which our algorithms effectively compute the solution, we systematically increased λ. For values of λ up through 100 (which is

the same as a Weissenberg number of 100, according to the definition taken by Trebotich et. al. [26]), we observed that the results were physically reasonable. Within this regime, we were able to effectively compute the solution to the linear system with small remaining residual. Results were qualitatively similar to those shown in Fig. 9. For $\lambda = 300$, we were able to evolve the calculation for a considerable length of time, however, once the viscoelastic effects became dominate (roughly corresponding to the time when the bubble started to retract), instabilities started to quickly build, and the linear solver was unable to effectively reduce the residual: this took place over the course of a few time steps, starting around time step 42000.

4.3 Collision of Viscoelastic Droplets

We finally consider the simulation of viscoelastic droplet collision. As shown in the first plot of Fig. 12, there are initially two identical pairs of major droplet and long satellite. The volumes of the major droplets and long satellites are 7.07 and 3.94 pico liters, respectively. The two long satellites are about 320 microns long. In Fig. 12, the velocity of the two major droplets are about 3.2m/sec. The head velocity of the two long tails is 1.65 while the tail velocity of them is 3.2m/sec. The shapes of the droplets for $\lambda = 0.4$ at different stage of the collision are shown in the rest plots of Fig. 12. It is interesting that the long tail evolves into a round satellite before colliding to the major droplets. One can see that the heads of the long tails proceed slowly from $t = 0$ to $t = 29.6\mu s$ although their mass centers move much faster. From $t = 29.6\mu s$ to $t = 47.6\mu s$, the heads of the two long tails actually retreat a little bit due to the fluid elasticity and surface tension. We did not see this phenomenon in a corresponding Newtonian simulation. A Newtonian droplet as long as the tail shown in the first plot of Fig. 12 would break into at least two satellites before any part of it hits onto the collided major droplets. The shape of the droplets after collision also depends on the initial velocity. Fig. 13 shows the results of droplet collision with all the initial velocities doubled. One can see that a donut shape is formed at $t = 35.6\mu s$.

Acknowledgements

We would like to thank Dr. Ann Almgren, Dr. John Bell, Dr. David Trebotich, and Prof. David Chopp for many valuable conversations.

References

[1] I. D. Aleinov, E. G. Puckett, and M. Sussman, "Formation of Droplets in Microscale Jetting Devices," *Proceedings of ASME FEDSM'99*, San Francisco, California, July 18-23, 1999.

[2] Ann S. Almgren, John B. Bell, and William G. Szymczak, "A Numerical Method for the Incompressible Navier-Stokes Equations Based on an Approximate Projection," *SIAM J. Sci. Comput.*, **17**(2), pp. 358-369, 1996.

[3] Ann S. Almgren, John B. Bell, and William Y. Crutchfield, "Approximate Projection Methods: Part I. Inviscid Analysis," *SIAM J. Sci. Comput.*, **22**(4), pp. 1139-59, 2000.

[4] John B. Bell, Phillip Colella, and Harland M. Glaz, "A Second-order Projection Method for the Incompressible Navier-Stokes Equations," *Journal of Computational Physics*, **85**(2), pp. 257-283, 1989.

[5] John B. Bell and Daniel L. Marcus, "A Second-order Projection Method for Variable-Density Flows," *Journal of Computational Physics*, **101**, pp. 334-348, 1992.

[6] John B. Bell, Jay M. Solomon, and William G. Szymczak, "A Projection Method for Viscous Incompressible Flow on Quadrilateral Grids," *AIAA Journal*, **32**(10), pp. 1961-1969, 1994.

[7] Y. C. Chang, T. Y. Hou, B. Merriman, and S. Osher, "A Level Set Formulation of Eulerian Interface Capturing Methods for Incompressible Fluid Flows," *Journal of Computational Physics*, **124**, pp. 449-464, 1996.

[8] Alexandre J. Chorin, "Numerical Solution of the Navier-Stokes Equations," *Math. Comput.*, **22**, pp. 745-762, 1968.

[9] Phillip Colella, "Multidimensional Upwind Methods for Hyperbolic Conservation Laws," *SIAM J. Sci. Stat. Comput.*, **87**, pp. 171-200, 1990.

[10] Denn, M.M., "Issues in Viscoelastic Fluid Mechanics", Annual Review of Fluid Mechanics, 22, pp. 13-32, 1990

[11] Mark Gerritsma, "Time Dependent Numerical Simulations of a Viscoelastic Fluid on a Staggered Grid," PhD thesis, 1996.

[12] Griebel, M., Dornseifer, T., and Neunhoeffer T. Numerical Simulation in Fluid Dynamics : A Practical Introduction. SIAM, (1998)45-49.

[13] Kupferman, R., Simulation of Viscoelastic Fluids, Couette-Taylor, J. Comp. Phys. 147 (1998) 22-59.

[14] Mathematical Research in Materials Sciences, Opportunities and Perspectives, National Academy Press, 1993.

[15] Osher, S. and Sethian, J. A. Fronts Propagating with Curvature-Dependent Speed: Algorithms Based on Hamilton–Jacobi Formulations. *J. Comput. Phys.* **79**, (1988)12-49.

[16] Elbridge G. Puckett, Ann S. Almgren, John B. Bell, Daniel L. Marcus, and William J. Rider, "A High-order Projection Method for Tracking Fluid Interfaces in Variable Density Incompressible Flows," *Journal of Computational Physics*, **130**, pp. 269-282, 1997.

[17] Sakai, S. Dynamics of Piezoelectric Inkjet Printing Systems. *Proc. IS&T NIP* **16**, (2000)15-20.

[18] James A. Sethian, *An Analysis of Flame Propagation*, Ph.D. Dissertation, Department of Mathematics, University of California, Berkeley, CA, 1982.

[19] James A. Sethian, "Curvature and the Evolution of Fronts," *Commun. in Math. Phys.*, **101**, pp. 487-499, 1985.

[20] James A. Sethian, "Numerical methods for propagating fronts" in *Variational Methods for Free Surface Interfaces*, (eds. P. Concus & R. Finn), Springer-Verlag, NY, 1987.

[21] James A. Sethian, Level Set Methods and Fast Marching Methods, Cambridge University Press, 2nd Edition, 1999.

[22] Akira Sou, Kosuke Sasai, and Tsuyoshi Nakajima, "Interface Tracking Simulation of Ink Jet Formation by Electrostatic Force", Proceedings of ASME FEDSM'01, New Orleans, Louisiana, May 29 - June 1, 2001.

[23] Mark Sussman, Peter Smereka, and Stanley Osher, "Axisymmetric free boundary problems," *Journal of Computational Physics*, **114**, pp. 146-159, 1994.

[24] Mark Sussman and Peter Smereka, "Axisymmetric free boundary problems," *Journal of Fluid Mechanics*, **341**, pp. 269-294, 1997.

[25] Mark Sussman, Ann S. Almgren, John B. Bell, Phillip Colella, Louis H. Howell, and Michael L. Welcome, "An Adaptive Level Set Approach for Incompressible Two-phase Flow," *Journal of Computational Physics*, **148**, pp. 81-124, 1999.

[26] D. Trebotich, P. Colella, and G. H. Miller, "A Stable and Convergent Scheme for Viscoelastic Flow in Contraction Channels," *Journal of Computational Physics*, **205**, pp. 315-342, 2005.

[27] Jiun-Der Yu and Shinri Sakai, "Piezo Ink Jet Simulations Using the Finite Difference Level Set Method and Equivalent Circuit," IS&T-NIP19, pp. 319-322, New Orleans, LA, September 2003.

[28] Jiun-Der Yu, Shinri Sakai, and James A. Sethian, "A Coupled Level Set Projection Method Applied to Ink Jet Simulation," *Interfaces and Free Boundaries*, **5**, pp. 459-482, 2003.

[29] J. D. Yu, S. Sakai, and J. A. Sethian, "A coupled Quadrilateral Grid Level Set Projection Method Applied to Ink Jet Simulation," *Journal of Computational Physics*, **206**(1), pp. 227-251, 2005.

[30] Jingyi Zhu and James Sethian, "Projection Methods Coupled to Level Set Interface Techniques," *Journal of Computational Physics*, **102**, pp. 128-138, 1992.

List of Tables

List of Figures

Mesh number	25×350	50×700	75×1050	100×1400
Time to pinch off	9.0002	9.0240	9.0388	9.0356

Table 1: The time of pinch off from various meshes.

Mesh number	25×350	50×700	75×1050	100×1400
t=4.80	1.240	1.267	1.273	1.272
t=6.40	1.036	1.087	1.094	1.094
t=8.00	0.998	1.044	1.049	1.050
t=9.60	0.996	1.053	1.060	1.062

Table 2: Droplet head velocities from various meshes.

Mesh number	25×350	50×700	75×1050	100×1400
t=9.24	0.6774	0.7021	0.7108	0.7110
t=9.56	0.6647	0.7001	0.7097	0.7099
t=9.88	0.6539	0.6982	0.7085	0.7088
t=10.20	0.6419	0.6965	0.7073	0.7081
t=10.52	0.6295	0.6949	0.7063	0.7074

Table 3: Droplet volumes from various meshes.

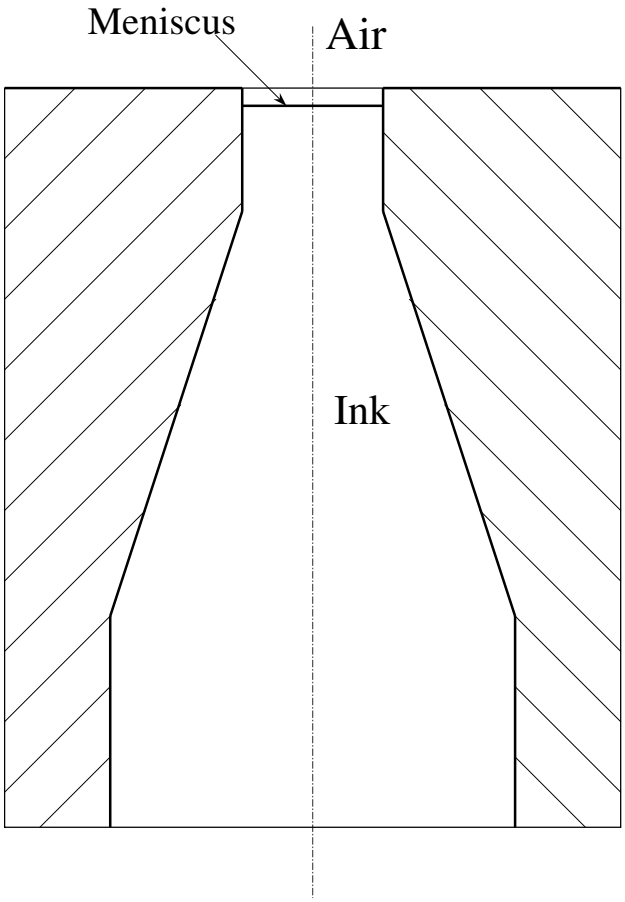

Figure 1: The cross section view of an ink jet nozzle.

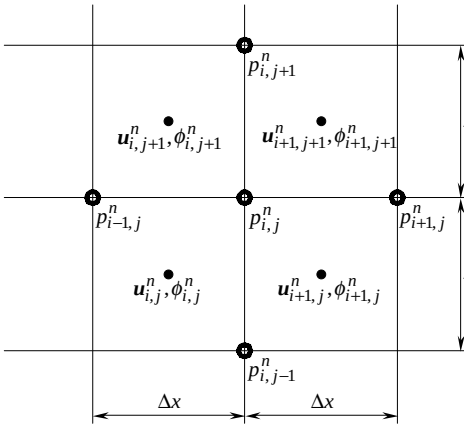

Discrete velocity field, pressure and level set

Figure 2a

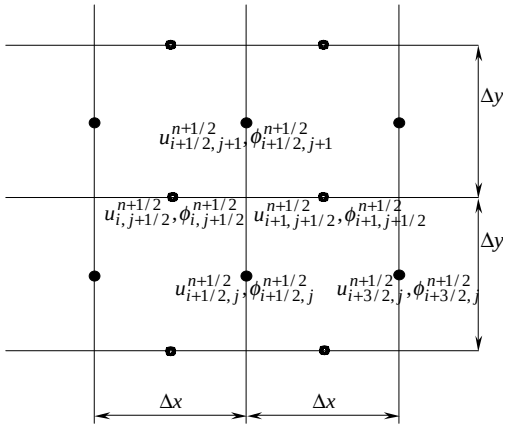

Intermediate velocity field and level set

Figure 2b

Figure 2: Location of Variables

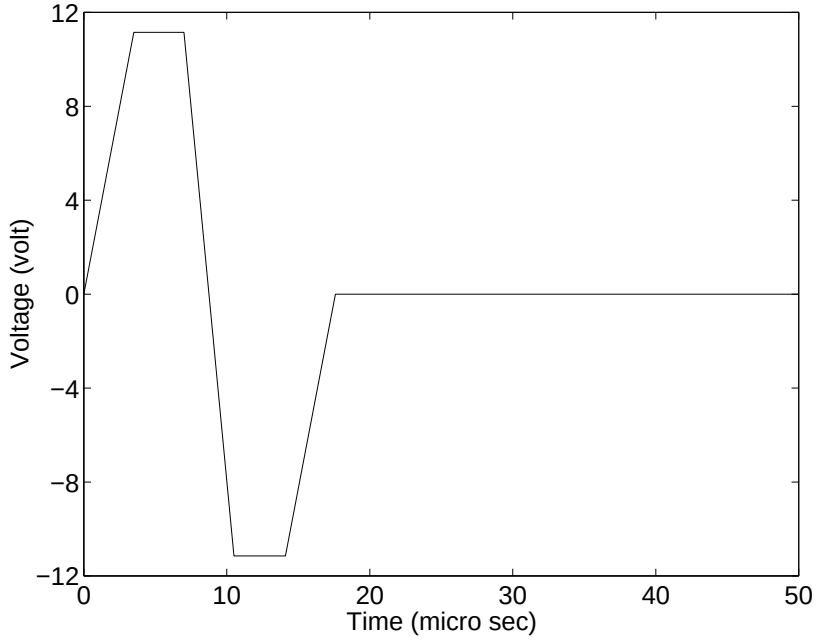

Figure 3: A typical ink jet driving voltage.

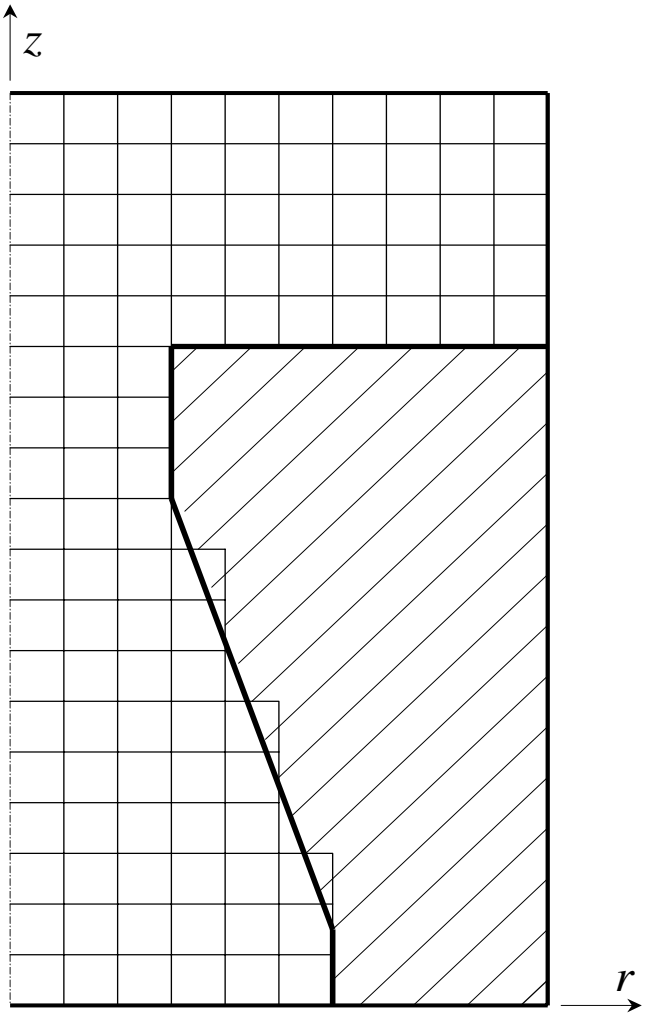

Figure 4: The zig-zag pattern due to rectangular mesh.

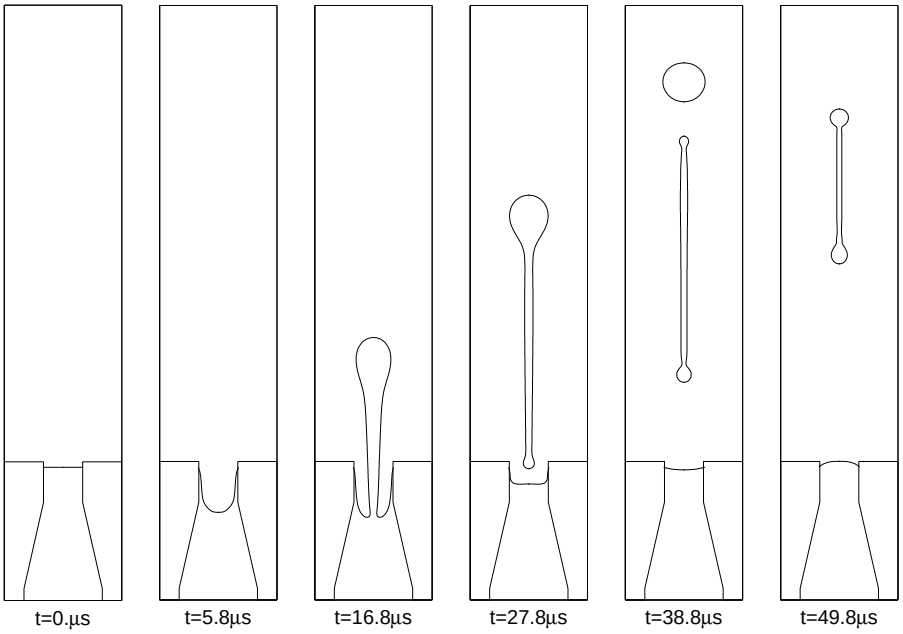

Figure 5: Droplet ejection (Newtonian).

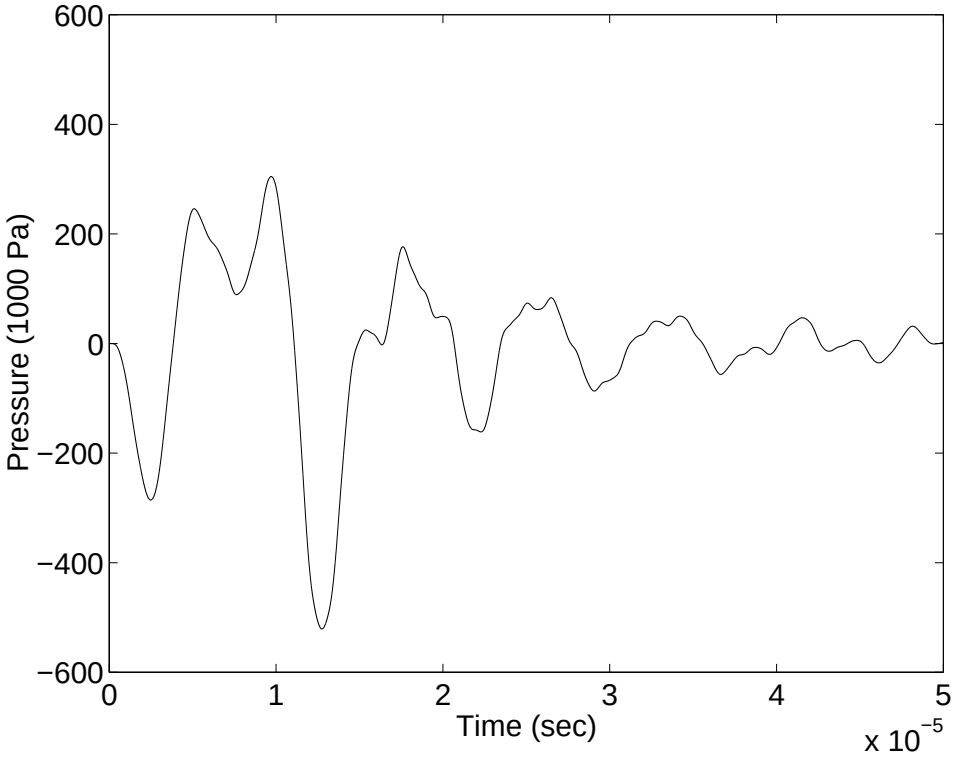

Figure 6: The corresponding inflow pressure for the Newtonian case ($\lambda = 0$).

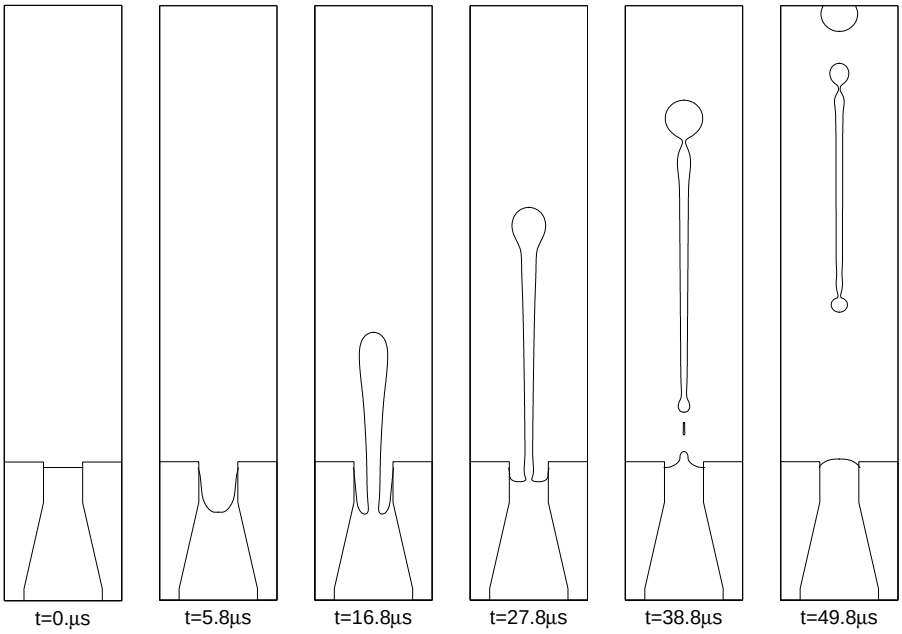

Figure 7: Droplet ejection ($\lambda = 0.4$).

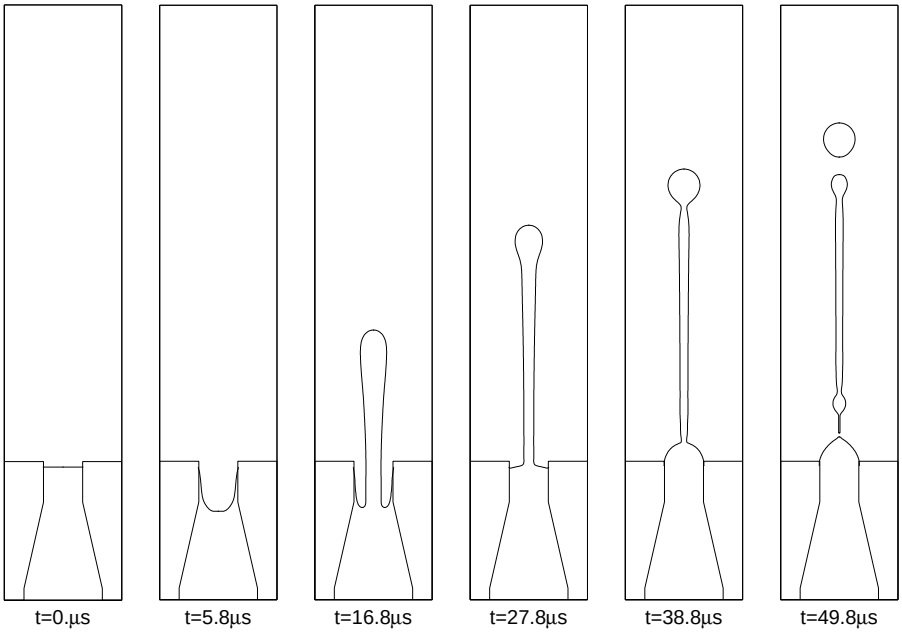

Figure 8: Droplet ejection ($\lambda = 1.0$).

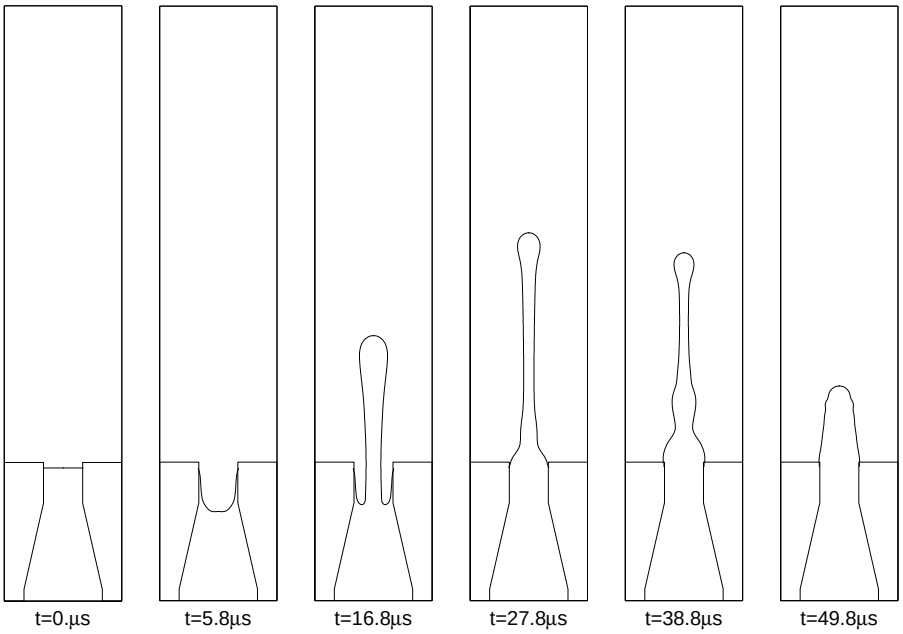

Figure 9: Droplet ejection ($\lambda = 3.0$).

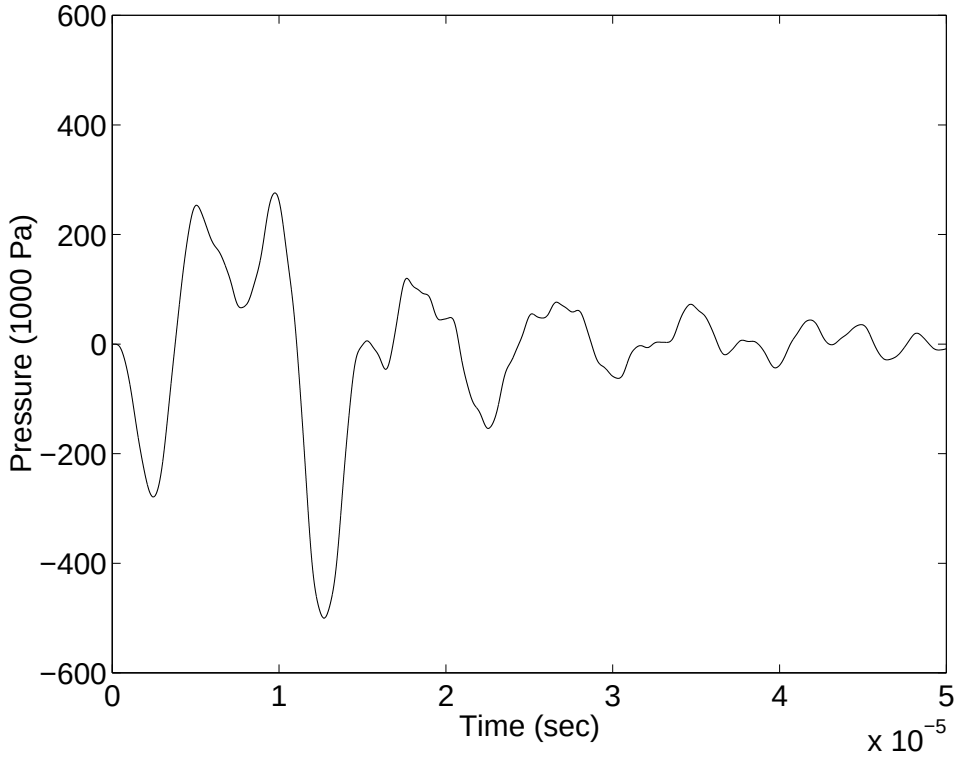

Figure 10: The corresponding inflow pressure for the case $\lambda = 3$.

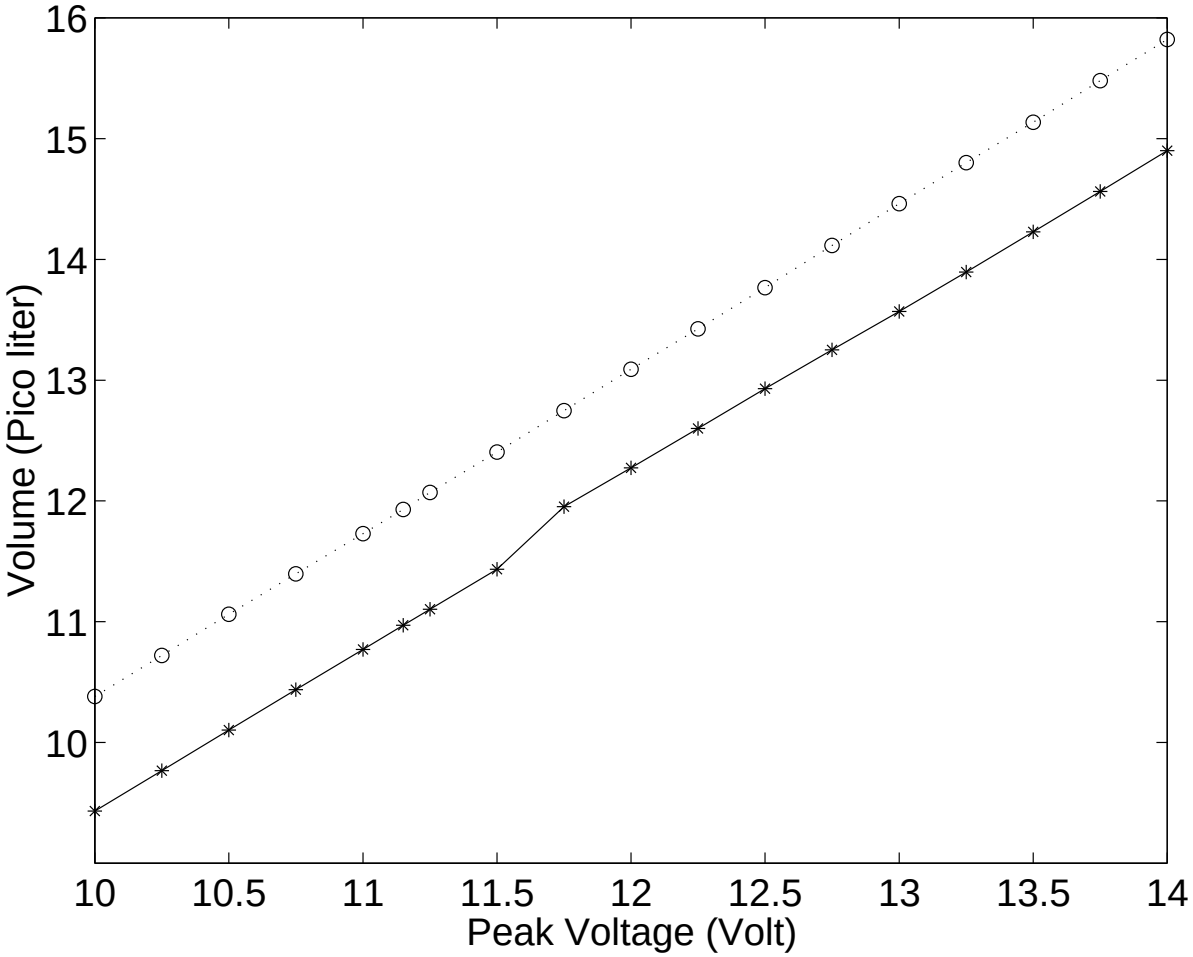

Figure 11: Droplet volume vs. peak voltage, dash line with circles for Newtonian case $\lambda = 0$ and solid line with asterisks for viscoelastic case $\lambda = 0.4$.

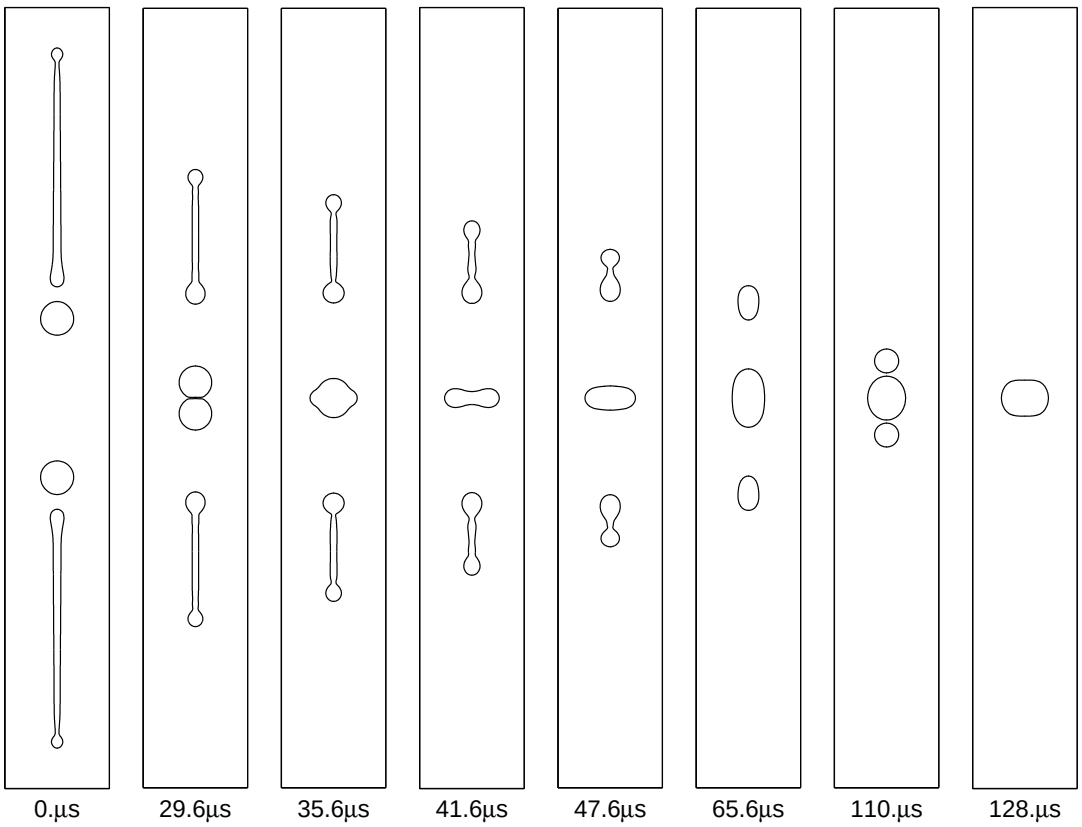

Figure 12: The collision of two pairs of major droplets and long satellites, $\lambda = 0.4$.

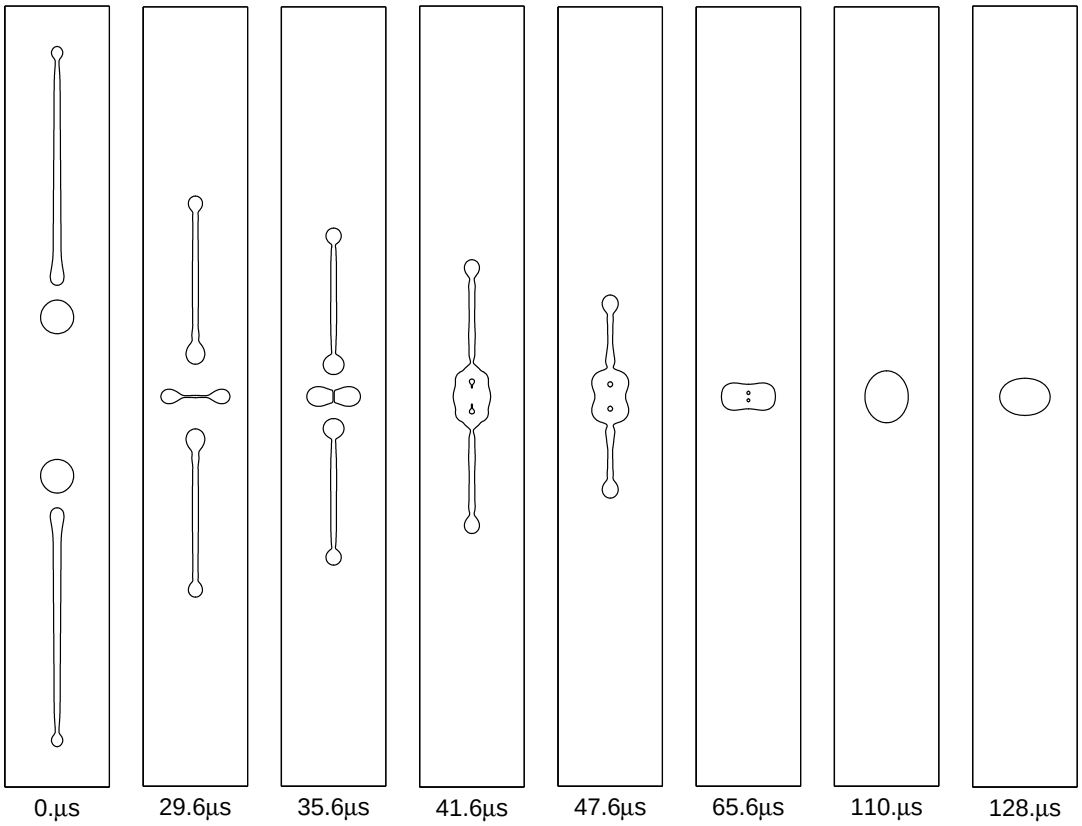

Figure 13: The collision of two pairs of major droplets and long satellites with velocities doubled, $\lambda = 0.4$